J. Fluid Mech. (2020), *vol*. 901, A1. © The Author(s), 2020.
Published by Cambridge University Press
doi:10.1017/jfm.2020.489

How shape and flapping rate affect the distribution of fluid forces on flexible hydrofoils

Paule Dagenais[1] **and Christof M. Aegerter**[1],†

[1]Physik-Institut, University of Zurich, Winterthurerstrasse 190, 8057 Zurich, Switzerland

(Received 29 October 2019; revised 11 May 2020; accepted 14 June 2020)

We address the fluid–structure interaction of flexible fin models oscillating in a water flow. Here, we investigate in particular the dependence of hydrodynamic force distributions on fin geometry and flapping frequency. For this purpose, we employ state-of-the-art techniques in pressure evaluation to describe fluid force maps with high temporal and spatial resolution on the deforming surfaces of the hydrofoils. Particle tracking velocimetry is used to measure the three-dimensional fluid velocity field, and the hydrodynamic stress tensor is subsequently calculated based on the Navier–Stokes equation. The shape and kinematics of the fin-like foils are linked to their ability to generate propulsive thrust efficiently, as well as the accumulation of external contact forces and the resulting internal tension throughout a flapping cycle.

Key words: flow–structure interactions

1. Introduction

The interplay between fins shapes, elastic properties, hydrodynamic forces and passive and controlled kinematics is the subject of persistent and active research (Videler 1975; Geerlink & Videler 1986; Tangorra *et al.* 2007; Lauder 2015; Puri *et al.* 2018). Replicating the flexible fins or the body of fish using hydrofoils with controlled motion programs has proven a powerful tool to investigate the kinematics and propulsive forces of swimmers (Shelton, Thornycroft & Lauder 2014). Methods to quantify the fluid velocity field are typically based on imaging tracer particles seeded into the flow corresponding to particle imaging velocimetry (PIV) or particle tracking velocimetry (PTV) (Maas, Gruen & Papantoniou 1993; Dracos 1996; Raffel *et al.* 1998; Pereira *et al.* 2006). The vortex wakes and thrust production of flapping foils with various geometries and flexibilities have been extensively characterized in the literature (Triantafyllou, Techet & Hover 2004; Godoy-Diana, Aider & Wesfreid 2008; Bohl & Koochesfahani 2009; Kim & Gharib 2010; Green, Rowley & Smits 2011; David *et al.* 2012; Marais *et al.* 2012; Shinde & Arakeri 2014; David, Govardhan & Arakeri 2017; Lucas, Dabiri & Lauder 2017; Muir, Arredondo-Galeana & Viola 2017). Furthermore, many researchers have resorted to particle velocimetry experiments in order to quantify the flow field of aquatic animal appendages and bioinspired synthetic fins (Blickhan *et al.* 1992; Stamhuis & Videler 1995; Müller *et al.* 1997; Drucker & Lauder 1999; Lauder 2000; Müller, Stamhuis & Videler 2000; Drucker & Lauder 2001; Müller *et al.* 2001; Nauen & Lauder 2002*a*,*b*; Drucker

† Email address for correspondence: aegerter@physik.uzh.ch

& Lauder 2005; Müller & Van Leeuwen 2006; Tytell 2006; Lauder & Madden 2007; Tangorra *et al.* 2007; Müller, van den Boogaart & van Leeuwen 2008; Tytell, Standen & Lauder 2008; Tangorra *et al.* 2010; Flammang *et al.* 2011*a*,*b*; Dewey, Carriou & Smits 2012; Esposito *et al.* 2012; Ren *et al.* 2016*a*,*b*; Mwaffo *et al.* 2017).

The research field making use of PIV/PTV-based pressure evaluation covers a large collection of hydrodynamics problems, from micro-channel junction flow and turbine blades to animal locomotion (Gresho & Sani 1987; Baur & Köngeter 1999; Gurka *et al.* 1999; Jakobsen, Dewhirst & Greated 1999; Fujisawa *et al.* 2006; Liu & Katz 2006; van Oudheusden, Scarano & Casimiri 2006; Murai *et al.* 2007; van Oudheusden *et al.* 2007; van Oudheusden 2008; Windsor 2008; Jardin, David & Farcy 2009; Lorenzoni *et al.* 2009; Khodarahmi *et al.* 2010; de Kat & van Oudheusden 2012; Ragni, van Oudheusden & Scarano 2012; de Kat & Ganapathisubramani 2013; van Oudheusden 2013; Panciroli & Porfiri 2013; Dabiri *et al.* 2014; Joshi, Liu & Katz 2014; Tronchin, David & Farcy 2015; Lucas *et al.* 2017; McClure & Yarusevych 2017; Mwaffo *et al.* 2017). Accurate and non-invasive methods to measure the fluid forces directly on the surface of flapping fins are essential to investigate the mechanisms of underwater propulsion. In the present work, we combine fluid velocity measurements from three-dimensional (3-D) particle tracking velocimetry with hydrodynamic stress calculations based on the Navier–Stokes equation to obtain well-resolved dynamic maps of fluid forces on the surface of flexible fin-like foils operating in different flow regimes. We address the long-standing question of how the geometry and kinematics of oscillating hydrofoils influence their spatio-temporal distributions of hydrodynamic forces. We focus on the effects of flapping frequency, width, length and edge curvature (straight versus bilobed). This approach offers a framework to investigate how specific morphological and kinematic features can constitute an advantage for certain hydrodynamic functions. The implications of this study reach into the fields of animal aquatic locomotion, as well as the engineering design of biomimetic underwater vehicles. Such propulsive systems are gaining importance due to their potential applications in the monitoring, maintenance and exploration of underwater environments (Low & Willy 2006; Lauder *et al.* 2007; Low 2007; Zhou & Low 2012; Qing Ping *et al.* 2013).

2. Material and methods

2.1. *Particle tracking velocimetry*

We use a three-dimensional, three-component particle tracking velocimetry approach to quantify the flow generated by the synthetic fins. Technical aspects of three-dimensional PTV are well described in Pereira *et al.* (2006). The basic principle of PTV relies on tracer particles seeded in the flow, illuminated by a laser beam and imaged at regular time intervals to track the position of each particle, allowing the subsequent reconstruction of the fluid velocity field. Because the aim is to calculate the hydrodynamic stress tensor from the velocity fields, this experimental method presents several benefits compared to other techniques such as tomographic or scanning stereo-PIV, the most outstanding one being the possibility to instantaneously capture the whole flow volume, allowing for the straightforward reconstruction of the 3-D velocity vectors everywhere inside that volume.

The different components of the experimental set-up are shown in figure 1 with their technical specifications. The working fluid is water and the seeding tracers are polyimide particles with a diameter of $\sim$50 μm, which have been used in previous particle velocimetry experiments to investigate the flow fields generated by fish fins (Flammang *et al.* 2011*a*). The measurement volume in our experiments is 50 mm $\times$ 50 mm $\times$ 20 mm,

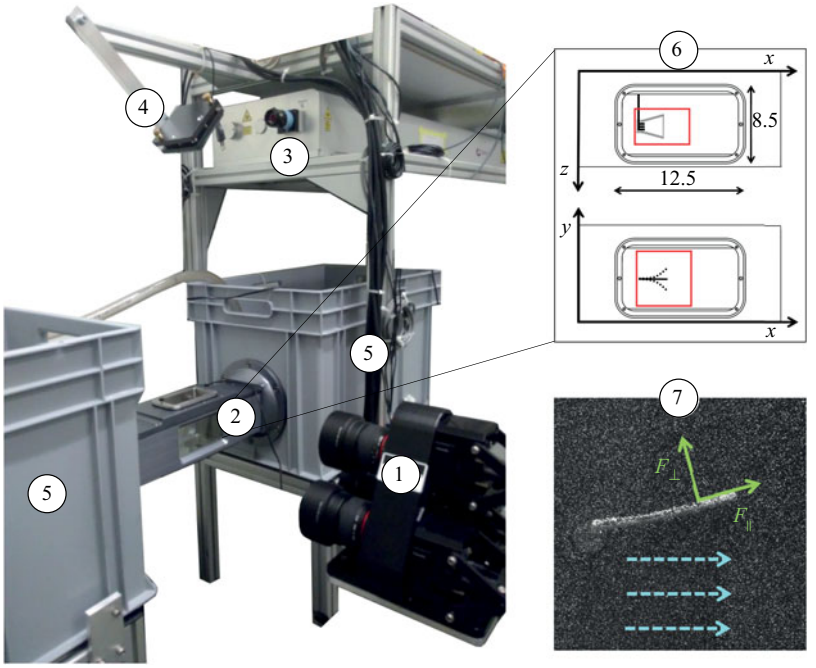

FIGURE 1. Experimental set-up: (1) camera triplet (4 MP, 85 mm lenses, sensor size 11.3 mm × 11.3 mm, magnification 0.3, max. frequency 180 Hz) arranged in a triangular configuration on a plate located at ∼465 mm from the middle of the (2) flow chamber, illuminated by a (3) laser beam (double-pulsed, Nd:YAG, wavelength 532 nm, max. 120 mJ pulse^{-1}) expanded by a pair of cylindrical lenses and deflected by (4) a mirror. (5) Recirculating system composed of two tanks (total volume of ∼160 l) and a pump connected to a pipe. (6) Sketch of the flow chamber with inner dimensions (in mm), top view (x–z plane) and frontal view (x–y plane), measurement volume (∼ 50 mm × 50 mm × 20 mm) indicated with red rectangles, enclosing the trapezoidal fin. (7) Example of an image captured by one of the three cameras, with tracer particles and hydrofoil midline clearly visible (direction of the free-stream indicated by blue dashed arrows and direction of the normal and tangential forces indicated by green arrows).

with an approximate number of 8×10^4 seeding particles inside that interrogation domain. Three cameras mounted on a plate in a triangular arrangement are used to record the 3-D fluid velocity vectors $\boldsymbol{u} = (u_x, u_y, u_z)$. The flow chamber has transparent walls on three sides and a fixation wall on one side for inserting the fin model, actuated with a servomotor fixed outside the chamber. The hydrofoils are mounted horizontally inside the tunnel, with their rotation axis parallel to the z axis and perpendicular to the cameras plate. A frontal perspective would make the detection of the particles more arduous in front of the fin surface. Water tanks are connected to both sides of the flow chamber in a recirculating system, and a pump pushes water inside a pipe from one tank to the other to control the upstream fluid velocity. A flow straightener is installed at the inlet of the tunnel to insure laminar incoming stream. All the experiments were performed using the V3V-9800 system (TSI Incorporated), which is characterized in Lai *et al.* (2008). The laser double pulse timing and the cameras capturing frequency are synchronized in a method called frame straddling: the time difference between a pair of position fields is determined by the time difference between a pair of laser pulses ($\delta t = 2.5$ ms), and the rate at which velocity fields are recorded (80 Hz) is half the camera acquisition frequency, yielding a time separation of

$\Delta t = 12.5$ ms between the velocity fields. The reconstruction of the particles positions is based on a 2-D Gaussian fit of the particles intensity distributions and a triplet search algorithm is used for the 3-D positions fields. The velocity vectors are computed by tracking the particle displacements between subsequent laser pulses, using a relaxation method to achieve a probability-based matching. These processing steps are conducted using the V3V software (version 2.0.2.7). An appropriate combination of median filter, velocity range and smoothing filter was applied to the raw velocity fields to reduce the noise level and remove the worst outliers. Moreover, a mask is applied over the hydrofoil during image processing to avoid detecting ghost particles inside its boundary. Finally, the raw vectors are interpolated on a regular 3-D grid using Gaussian interpolation, yielding a final spatial resolution of 0.75 mm in each direction. Temporal and spatial resolutions were chosen along recommendations offered in previous studies where the flow velocity field was used to compute hydrodynamic pressure (de Kat & van Oudheusden 2012; Dabiri *et al.* 2014; Wang *et al.* 2017). The grid points inside the hydrofoil boundary, where no particle is detected owing to the mask, are not attributed a velocity value and are not involved in the hydrodynamic stress calculation. The closest grid points to the real fin boundary define a virtual boundary, where the surface distributions of hydrodynamic forces are evaluated.

The foil midline is visually tracked over time in the x–y plane (see label 7 of figure 1). For each time frame, points are manually superimposed on the fin midline and fitted with a polynomial of degree 2. The 3-D hydrofoil is reconstructed based on that fitted quadratic curve, assuming that deflection occurs only along one axis. The virtual object has a larger width than the actual foil (0.725 mm away from the real surface on each side) owing to the fact that the particles cannot be resolved directly at the fluid–solid interface. In order to evaluate if the reconstructed foil boundary is sufficiently close to the real surface where we want to extract the hydrodynamic pressure, we used the criterion that the virtual surface should be located within the fluid boundary layer. Based on the assumption of a laminar boundary layer, its thickness can be expressed as (in the simplified case of a flat plate, with U being the fluid velocity far from the plate and ν being the kinematic viscosity of the fluid) (Prandtl 1952)

$$\delta = 5\sqrt{\frac{\nu x}{U}}. \tag{2.1}$$

We could estimate that the thickness of the fluid boundary layer is >1 mm everywhere on the fin except at the most proximal region ($<10\,\%$ of the fin length). The virtual surface thus remains inside the boundary layer of the real object. Even though the boundary layer of an oscillating fin involves more complex phenomena such as turbulence, separation and reattachment (Obremski & Fejer 1967; Kobashi & Hayakawa 1980; Arnal 1984; Incropera *et al.* 2007; Kunze & Brücker 2011), these flow effects would tend to make the boundary layer extend further away from the solid surface. Therefore, the assumption of laminarity of the boundary layer gives a conservative estimate of the boundary layer width and thus allows us to verify that the virtual foil boundary provides an accurate representation of the real surface distributions. This point was verified in a previous study (Dagenais & Aegerter 2019), where we used a control volume analysis to compute the forces generated by a flapping fin in similar conditions, and showed that the results compared favourably to the integrated force distributions over the fin surfaces.

2.2. *Morphologies and kinematics of the fin models*

The synthetic fins are illustrated in figure 2 and characterized in table 1 and figure 3. Taking shape A_1 as the reference geometry, A_2 constitutes a shorter version and shape

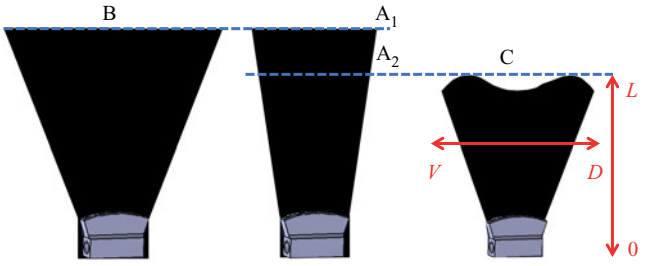

FIGURE 2. Four fin geometries under study. Principal axes of the fin are shown in red: proximo-distal axis (from 0 to L) and dorso-ventral axis (from V to D).

Shape	L (mm)	d (mm)	Re
A_1	25	14	1375
A_2	20	13	1100
B	25	24	1375
C	20	13	1062

TABLE 1. Parameters of the fin models: length (L), width at the tip (d, distance between lobes tips for shape C), and Reynolds number (Re).

B, a wider version. Shape C has the same length as shape A_2, but presents a bilobed trailing edge. The aspect ratio (AR) of a fin is defined as the square of the span (width at largest point) divided by the area. Even though the fin models do not mimic any fish species in particular, their geometries can be compared to caudal fins with low aspect ratios (AR = 0.84 for shape A_1, 1.03 for shape A_2, 1.67 for shape B and 1.1 for shape C). Examples include the *Schistura* genus, the *Oryzias* genus, the zebrafish (*Danio rerio*) and the platy fish (*Xiphophorus maculatus*), as shown in figure 3 (Sambilay 2005; Offen *et al.* 2008; Parichy *et al.* 2009; Naruse, Tanaka & Takeda 2011; Plongsesthee, Beamish & Page 2012; Bohlen *et al.* 2016; Kottelat 2017).

To produce the foils, a rigid cast of their negative form was 3-D printed, then liquid PDMS (polydimethylsiloxane) was poured inside the cast and the supporting rod was inserted at the base. The material was cured for 36 h at 58 °C. The resulting flexible membranes have a thickness of 0.55 mm. The properties of the cured PDMS can be found in the MIT material property database (http://www.mit.edu/6.777/matprops/pdms.htm). Most importantly, the mass density matches that of water. A cantilever deflection set-up was employed by S. Puri (University of Zurich) to characterize the elastic properties (see Puri 2018; Puri *et al.* 2018 for details), yielding a value of 0.8 MPa for the Young's modulus. An external velocity of $u_\infty = 55$ mm s^{-1} is imposed in all experiments, and the fins are actuated at their leading edge with a sinusoidal pitching motion with angular amplitude $\theta_0 = 11^\circ$ in all cases. Shape A_1 was selected to test the effects of pitching frequency, using $f_1 = 1.9$ Hz, $f_2 = 2.8$ Hz and $f_3 = 3.7$ Hz. The natural frequency of this fin model (first mode) was estimated by releasing it from a rest position and measuring the decaying oscillation of its tip (in water). A value of 2.4 Hz was found, in between the lowest and intermediate frequencies tested. For the experiments involving shapes A_2, B and C, frequency $f_2 = 2.8$ Hz is used.

Two dimensionless parameters allow us to characterize the flow regime of the hydrofoils. The Strouhal number (St) encompasses the propulsion dependence on tail oscillation. The

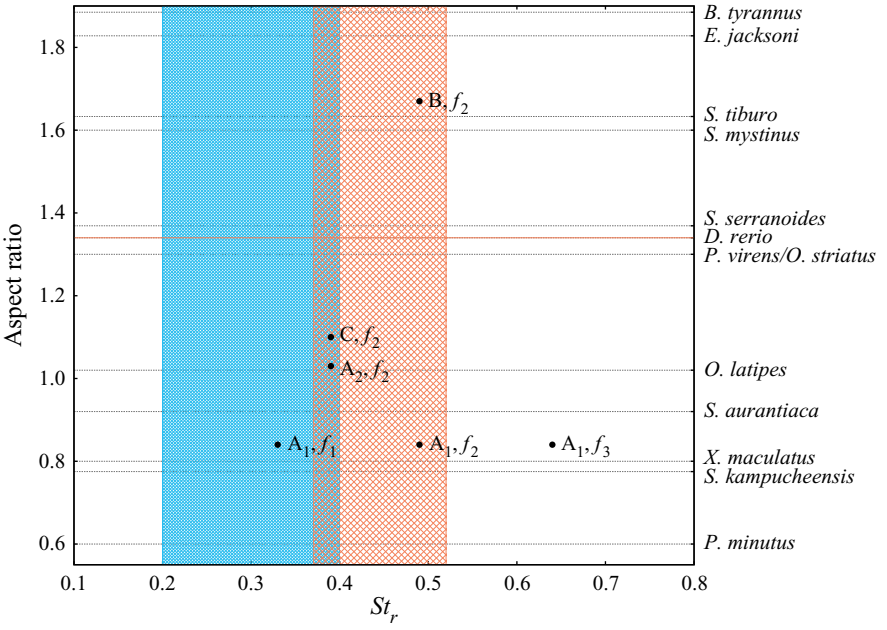

FIGURE 3. Black dots: aspect ratio and rigid Strouhal number (St_r, calculated based on the rigid projection of the peduncle) for each fin model. Horizontal lines: caudal fins aspect ratios for various fish species, derived from Sambilay (2005), Offen *et al.* (2008), Parichy *et al.* (2009), Naruse *et al.* (2011), Plongsesthee *et al.* (2012), Bohlen *et al.* (2016) and Kottelat (2017). Dashed blue zone: range of Strouhal numbers typically associated with efficient propulsion for flapping foils (Triantafyllou *et al.* 2000; Taylor *et al.* 2003). Dashed pink zone: range of Strouhal numbers for the adult zebrafish caudal fin, derived from Parichy *et al.* (2009), Palstra *et al.* (2010) and Mwaffo *et al.* (2017).

Reynolds number (Re) describes the viscous versus inertial effects and determines the transition from a laminar to a turbulent flow. These parameters are based on the kinematic viscosity of water (ν), the external fluid velocity ($U = u_\infty$), the foil length (L), the flapping frequency (f) and the tip excursion amplitude (A)

$$Re = \frac{UL}{\nu}, \quad St = \frac{fA}{U}. \tag{2.2a,b}$$

Caudal fins found in nature are extremely diverse and cover a vast range of flow parameters, depending on species but also on developmental stage and behaviour. The swimming velocities catalogued in the literature usually correspond to the maximal speeds which fish can sustain for a short time only, yielding Re from 10^4 to 5×10^6 (using the animal body length) (Wardle 1975; Yates 1983; Vogel 1994). These high values are not representative of slower gaits at which fish can also operate in natural conditions (Bainbridge 1960; Weerden, Reid & Hemelrijk 2013). For example, based on the vast literature about zebrafish hydrodynamics, it can be estimated that this species operates at Re in the range [390–2600] (using the caudal fin length to allow direct comparison with isolated hydrofoils) (Parichy *et al.* 2009; Palstra *et al.* 2010; Mwaffo *et al.* 2017). In the present study, Re is situated within [1062–1375] (table 1). Although not characteristic of fast bursts or maximal velocity locomotion, this flow regime can be compared to the case of fish cruising at approximately 0.5 to 0.9 body lengths per second, pertinent for

certain species (Sambilay 2005) and specific behaviours such as foraging, chemotaxis and exploration.

Furthermore, studies have demonstrated that fundamental flow features of flapping fin propulsion can be captured by experiments and simulations performed at *Re* lower than values typically measured for fast swimming fish, down to of the order of 10^3 (Lauder *et al.* 2005; Bozkurttas *et al.* 2006; Buchholz & Smits 2006; Kern & Koumoutsakos 2006; Mittal *et al.* 2006; Bozkurttas *et al.* 2009; Liu *et al.* 2017). Indeed, for sufficiently high *Re* ($\geq 10^3$), this parameter plays a minor role compared to *St* in defining the flow topology (Lentink 2008; Green *et al.* 2011).

In the case of flexible foils, *St* depends on the tip excursion amplitude and has to be measured rather than fixed prior to the experiments. Therefore, we additionally define the rigid Strouhal number (St_r), an input parameter based on the excursion amplitude of an equivalent rigid fin (same length and angular amplitude at the base). For the six experimental cases, we obtain St_r in the range [0.33–0.64] (figure 3). Strouhal numbers between 0.2 and 0.4 usually yield the highest propulsion efficiency (Triantafyllou, Triantafyllou & Yue 2000; Taylor, Nudds & Thomas 2003). Nevertheless, wider ranges of *St* within [0.2–0.7] were reported in various fish species and for different developmental stages (Eloy 2012; Eloy 2013; Weerden *et al.* 2013; Xiong & Lauder 2014; Van Leeuwen, Voesenek & Müller 2015; Link *et al.* 2017). For example, adult zebrafish flap their caudal fins with *St* in a window of [0.37–0.52], depending on their swimming mode (Parichy *et al.* 2009; Palstra *et al.* 2010; Mwaffo *et al.* 2017).

Aside from their pertinence in the fish world, the experimental parameters (AR, *Re* and *St*) are similar to those selected in previous research about fluid–structure interactions of flapping foils (Lauder *et al.* 2005; Godoy-Diana *et al.* 2008; Dai *et al.* 2012; Marais *et al.* 2012; Dewey *et al.* 2013; Quinn, Lauder & Smits 2014; Shinde & Arakeri 2014; Quinn, Lauder & Smits 2015; David *et al.* 2017; Floryan *et al.* 2017; Liu *et al.* 2017; Rosic *et al.* 2017; Zhu *et al.* 2017). We explore a specific portion of the flow parameter space to understand how propulsive efficiency and surface distributions of hydrodynamic forces depend on shape and frequency at relatively low Reynolds numbers, a topic of high interest in the field of fin propulsion and for the practical design of underwater vehicles relying on bio-inspired undulating membranes.

2.3. *Calculations*

Based on the PTV-velocity fields, the total hydrodynamic stress tensor $\boldsymbol{s}$ is calculated at each node in the 3-D domain, which is the sum of the scalar pressure field p (multiplied with the identity matrix and a factor -1) and the viscous stress tensor $\boldsymbol{\tau}$

$$s_{ij} = -p\delta_{ij} + \tau_{ij}. \tag{2.3}$$

The viscous stress tensor depends only on the spatial derivatives of the velocity field (where μ is the dynamic viscosity)

$$\tau_{ij} = \mu\left(\frac{\partial u_i}{\partial x_j} + \frac{\partial u_j}{\partial x_i}\right). \tag{2.4}$$

Although it was included in the calculation, the viscous stress is much smaller than the pressure in the present case. Indeed, the fins operate in the inertial flow regime ($Re > 1000$), although theoretically very close to the transitional range $300 < Re < 1000$ (McHenry & Lauder 2005), where the normal stress component (dominated by the

pressure) is typically larger than the viscous tangential stresses by at least two orders of magnitude.

The pressure evaluation is based on the Navier–Stokes equation (Whitaker 1968; Aris 1990)

$$\rho \frac{\mathrm{D}\boldsymbol{u}}{\mathrm{D}t} = -\boldsymbol{\nabla} p + \boldsymbol{\nabla} \cdot \boldsymbol{\tau} + \rho \boldsymbol{g}. \tag{2.5}$$

The last term on the right corresponds to any type of body force such as gravity; it is included in the pressure term and omitted in the remaining development. The left side of the equation contains the material acceleration D/Dt. This term is evaluated in the Lagrangian frame, namely in the reference frame of the advected particle (Dabiri *et al.* 2014). Each component of the pressure gradient can be calculated from the Navier–Stokes equation

$$\frac{\partial p}{\partial x_i} = \left(-\rho \left(\frac{\partial}{\partial t} + \sum_j u_j \frac{\partial}{\partial x_j} \right) + \mu \sum_j \frac{\partial^2}{\partial x_j^2} \right) u_i. \tag{2.6}$$

Instantaneous pressure fields are reconstructed through direct integration of the above equation with appropriate boundary conditions. We performed the pressure calculation using the queen2 algorithm from Dabiri *et al.* (2014), available at http://dabirilab.com/software/. A null pressure value is assumed on the external boundary of the domain, in the undisturbed flow. The validity of that assumption relies on the conditions $H/D \geqslant 2$, where H is half of the domain size (Dabiri *et al.* 2014). Substituting the tip excursion amplitudes for the characteristic dimension D, we conclude that our experiments lie just above that limit. For each node inside the domain, the pressure gradient is integrated along eight different paths (horizontal, vertical or diagonal) originating on the outside contour. The median from the eight resulting pressure values is finally selected. This algorithm offers the advantage of reasonable computation time even for large domains. The crucial step in the pressure calculation lies in the determination of the material Lagrangian acceleration. In the queen2 algorithm, a so-called pseudo-tracking scheme is applied. The position of a particle at an instant t_{i+1} is approximated based on its initial location $\boldsymbol{x}_p(t_i)$ and the velocity evaluated at this location, averaged between instants t_i and t_{i+1}. The velocity of the particle at its estimated forward position at time t_{i+1} is then employed to evaluate its acceleration at time t_i. The pressure gradient is evaluated in a quasi-3-D manner, using in-plane velocity derivatives only, but combining integration paths in both the x–y and the x–z planes. The details of the calculation are presented in Dabiri *et al.* (2014).

The total hydrodynamic stress tensor (2.3) is projected on the surface of the solid object to obtain a stress vector, which is the total force per unit area generated by the fluid on the foil. Each i-component of the hydrodynamic stress vector acting on a surface with a unit normal vector $\hat{e}_n = (n_x, n_y, n_z)$ (oriented outwards) is expressed as

$$S_i(\boldsymbol{x}, t, \hat{n}) = s_{ij}(\boldsymbol{x}, t) \cdot n_j. \tag{2.7}$$

In § 3, two types of distributions are presented: (i) instantaneous forces (per unit length), obtained by the integration of the surface stress maps along the dorso-ventral axis, at five selected time points covering half a period of oscillation, and (ii) period-averaged stress maps, where the normal stress is averaged either in absolute value or with its sign. In each experiment, the flow field is collected over three flapping periods and 30 pairs of velocity fields (10/period) are selected for the evaluation of hydrodynamic forces. Instantaneous distributions are averaged over six equivalent time frames (considering the symmetry

Shape	Frequency	$\Delta\phi$ (T)	A (mm)	$\overline{u}_{vol}$ (mm s^{-1})	$\overline{u}_{fin}$ (mm s^{-1})	St	η
A_1	f_1	0.11	11.0	52.6	48.3	0.37	0.14
A_1	f_2	0.18	12.0	54.5	54.8	0.61	0.17
A_1	f_3	0.32	10.3	56.5	58.4	0.69	0.17
A_2	f_2	0.08	8.0	55.3	53.8	0.40	0.13
B	f_2	0.36	7.7	46.4	47.4	0.39	0.19
C	f_2	0.07	7.5	56.7	61.4	0.38	0.10

TABLE 2. Kinematics and flow regime of the hydrofoils: phase lag between peduncle and tip angles ($\Delta\phi$, in fraction of a period), total amplitude covered by the fin tip over a period (A), streamwise velocity component averaged over three periods ($\overline{u}_{vol}$, averaged over the whole volume, and $\overline{u}_{fin}$, averaged over the virtual surface enclosing the fin), Strouhal number (St) and efficiency ratio (η).

between the left and right strokes). The period-averaged distributions are based on the 30 time frames. The instantaneous force (per unit length) is decomposed into the x and y directions, yielding the thrust F_x and lateral force F_y acting on the fin. The thrust force corresponds to the useful power spent by the fin (when it points in the negative x direction, propelling the system upstream). The lateral forces correspond to the wasted power. Hence, we define the efficiency ratio as the power invested by the fin into useful thrust divided by the total rate of work done on the fluid

$$\eta = \frac{\left|\langle F_x \rangle\right| \langle \overline{u}_{fin} \rangle}{\left|\langle F_x \rangle\right| \langle \overline{u}_{fin} \rangle + \langle \left| F_y \right| \rangle 2Af}. \tag{2.8}$$

This definition is equivalent to the Froude efficiency: it measures the ability of the fin to convert work into upstream propulsion (Eloy 2013; Quinn *et al.* 2015). The over lines indicate a spatial average and the brackets indicate a time average over a period. Note that F_x is averaged with its sign; the absolute value is applied after averaging, whereas F_y is averaged in absolute value directly because the fin is wasting energy due to lateral forces from both sides. The fluid velocity is averaged over the foil virtual boundary rather than over the whole volume, in order to better capture the specific ability of each hydrofoil to generate downstream fluid motion (see table 2). This classification based on η is compared to the usual efficiency classification based on the Strouhal number, where the window of efficient propulsion is considered to be [0.2,0.4] (Triantafyllou *et al.* 2000; Taylor *et al.* 2003).

Many authors have calculated the denominator of (2.8) for pitching fins (input power) as the period-averaged product of torque and angular velocity at the base (Dewey *et al.* 2013; Lucas *et al.* 2015, 2017; Quinn *et al.* 2015; Egan, Brownell & Murray 2016; David *et al.* 2017; Floryan *et al.* 2017; Rosic *et al.* 2017; Zhu *et al.* 2017). This efficiency metric is appropriate for hydrodynamic experiments where forces and torque sensors are placed at the attachment rod of the flapping propulsor. In the present study, no load cells are involved and all information about the forces imparted by the foil on the fluid are extracted solely from the flow velocity field. In this context, a definition of η based on local force components integrated on the fin surfaces is more suitable. A similar calculation using surface integration of hydrodynamic stresses was used in Liu *et al.* (2017).

The uncertainties on the pressure and force distributions can be obtained using error propagation arguments and an analysis of the inaccuracy on the Lagrangian path reconstruction (used in the material acceleration evaluation). The uncertainties on the particles positions in our PTV experimental set-up are $\sigma_x = \sigma_y \simeq 3.6$ µm and $\sigma_z \simeq 32$ µm, which imply velocity uncertainties of $\sigma_{u_x} = \sigma_{u_y} \simeq 0.002$ m s^{-1} and $\sigma_{u_z} \simeq 0.018$ m s^{-1}. Noise propagation from the velocity field to the material acceleration and to the integrated pressure field has been the object of many studies (Liu & Katz 2006; Violato, Moore & Scarano 2011; de Kat & Ganapathisubramani 2013; van Oudheusden 2013; Wang *et al.* 2017). We can derive an expression for the pressure uncertainty, relevant for the present calculation scheme. As a first step, we express the material acceleration uncertainty (with $a_i = \mathrm{D}u_i/\mathrm{D}t$) as a sum of the error propagated from the velocity field (first term under the square root) and the uncertainty from the Lagrangian path line reconstruction (second term)

$$\sigma_{a_i} = \sqrt{\frac{2\sigma_{u_i}^2}{\Delta t^2} + \left((\boldsymbol{\sigma}_u \cdot \nabla) u_i\right)^2}. \tag{2.9}$$

The pressure field is the result of a spatial integration, its uncertainty therefore depends on the spatial resolution Δx_i and on the number of nodes n crossed along the integration path. Moreover, the pressure integration algorithm involves a median polling among a collection of $N = 8$ paths, which reduces the uncertainty further by a factor of $\sqrt{\pi/2(N-1)}$ (Kenney & Keeping 1962, pp. 32–35, 52–54, 211–212). Because any of the x, y or z directions can be followed by the integration paths, the estimated pressure uncertainty is based on the average of errors in all three directions (Dagenais & Aegerter 2019)

$$\sigma_p = \frac{\rho}{3}\sqrt{\frac{\pi}{14}}\sum_{i=1}^{3} n\Delta x_i \sqrt{\frac{2\sigma_{u_i}^2}{\Delta t^2} + \left((\boldsymbol{\sigma}_u \cdot \nabla) u_i\right)^2}. \tag{2.10}$$

The local pressure uncertainties are propagated to the force uncertainties using classic error propagation through an integration step, and the resulting values are shown with error bars in § 3. Due to temporal and spatial averaging, these uncertainties are reduced by an additional factor of $\sqrt{N_{time} \times N_{spatial}}$; N_{time} is the number of time frames employed in the period average (6 or 30 for the instantaneous and period averaged distributions, respectively); $N_{spatial}$ is 1 for the instantaneous distributions and 20 in the case of the period-averaged curves of figure 11, which are spatially averaged over the left/right and dorsal/ventral symmetric sides of the fin, as well as over five dorso-ventral rows for each curve.

3. Results

3.1. *Hydrofoil kinematics*

The geometry and flapping frequency directly affect the fluid–structure interactions of the hydrofoils. The deflection profiles of the midlines along the course of a flapping cycle are shown in figure 4. The midline excursions are used to evaluate A, the tip amplitude, which is needed to calculate St. The phase lag between the peduncle and the tip ($\Delta\phi$) is determined by measuring the angle between the fin midline and the horizontal plane (at the peduncle and at the tip) at regular time points during the motion cycle. The results are listed in table 2. The largest phase lag is found for the wide fin geometry (shape B), with $\Delta\phi$ twice as large as for shape A_1. This tip recoil is associated with a smaller excursion

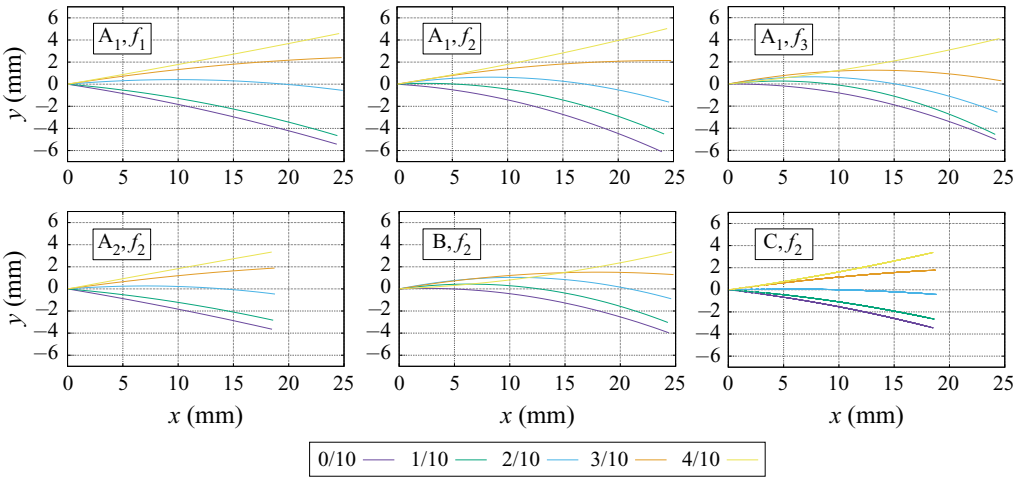

FIGURE 4. Hydrofoil midlines at five time points equidistant over half a period.

amplitude at the tip (A). Increasing the flapping frequency of shape A_1 induces a larger phase lag, but in this case, the diminution of the tip amplitude is less important. Almost no phase lag is found for the shorter fins, independently of the trailing edge geometry (shapes A_2 and C). The shorter geometries thus behave more like rigid fins. The capacity of each hydrofoil to generate streamwise fluid velocity can be analysed by averaging the value of u_x over multiple periods and the whole volume ($\overline{u}_{vol}$) or over the fins virtual boundary ($\overline{u}_{fin}$), the latter option displaying more obvious differences (see table 2). The highest streamwise velocity is produced by the bilobed short fin (shape C), followed by the long narrow fin flapping at maximal rate (shape A_1 at f_3). The slowest fluid velocity is observed in the case of the wider fin (shape B) followed by the long narrow fin flapping at minimal rate (shape A_1 at f_1). Based on the Strouhal numbers alone, we would anticipate that the foil shape A_1 with flapping frequencies f_2 and f_3 lie outside of the propulsive efficiency range [0.2, 0.4]. Nevertheless, the efficiency ratio η offers a different perspective on that classification, as will be shown in § 3.2.

3.2. *Spatio-temporal distributions of fluid forces*

The colour code of figures 5, 6 and 9 follows that of figure 4 in terms of time partition. Figure 5 illustrates the distributions of fluid forces (per unit length) in the x direction, acting on the fins, along their proximo-distal axis. Half a period is represented using five equidistant time points (naturally, the opposite half-period would produce symmetrical distributions). Negative values correspond to useful propulsive thrust as the system is pushed upstream. In all cases, the maximal amount of thrust is produced when the tip is leaving its maximal point and initiating its motion back towards the centre (time point 1/10 in green). The thrust then reduces gradually until time point 3/10 (orange), after which it increases again as the fin approaches the opposite extremity of its excursion (time point 4/10 in yellow). The maximal amount of thrust is generated by the long fin at maximal flapping rate (shape A_1 at f_3), followed by that same geometry at frequency f_2. The wider fin (shape B) also produces significant thrust although slightly lower than the narrow geometry. For these three cases, the maximal amount of force is generated by the most distal portion of the fin, peaking close to 80 % of the total length. The thrust is drastically reduced in the case of the shorter fin (shape A_2). In comparison, the short fin

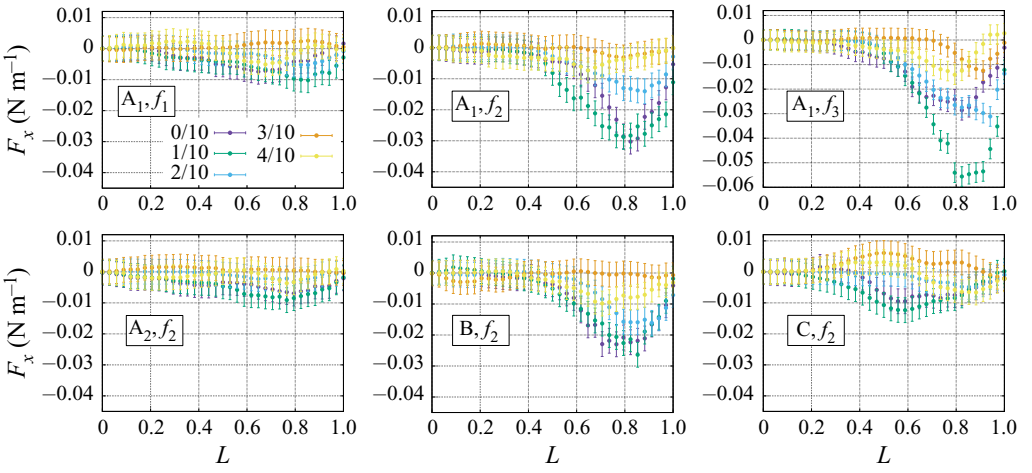

FIGURE 5. Thrust (x-component) force per unit length acting on the fin (in N m^{-1}), at five time points equidistant over half a period.

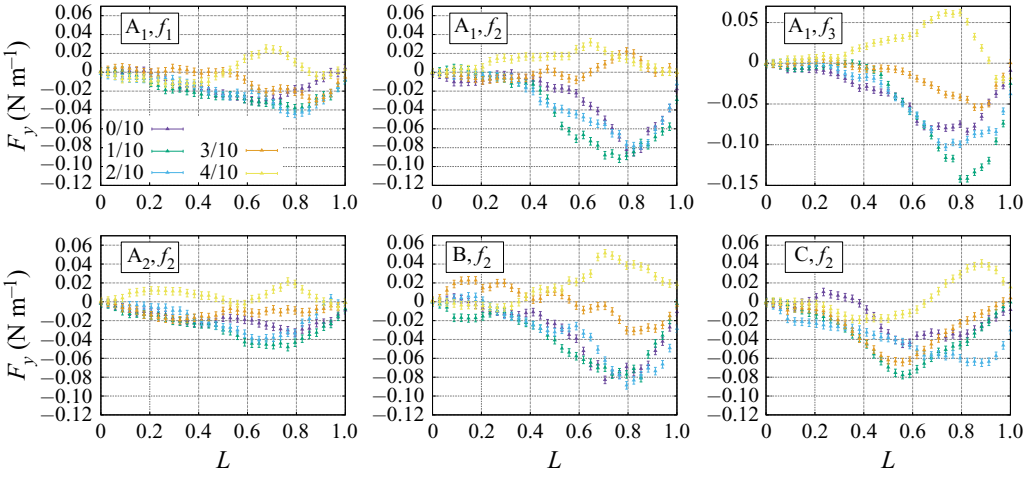

FIGURE 6. Lateral (y-component) force per unit length acting on the fin (in N m^{-1}), at five time points equidistant over half a period.

with bilobed edge (shape C) produces slightly larger amount of thrust at time points 0/10 and 1/10, but this is compensated by a positive distribution of F_x at time 3/10, detrimental to propulsion. In that specific case, the maximum amount of force is generated closer to the centre of the foil. The time evolution of the total force in the x direction (integrated over the whole fin surface) is shown in red in figure 7. Because of the symmetry between the left and right strokes of the fin, maximum thrust is generated twice per cycle.

Figure 6 presents the y component of the hydrodynamic force (per unit length) acting on the fin. This lateral force corresponds to wasted energy (not useful to propulsion). The most thrust-producing foils (shapes A$_1$ at f_3, A$_1$ at f_2 and shape B) are also the ones where the most energy in lost in accelerating fluid in the lateral direction. Moreover, the distribution on F_y is correlated to the distribution of F_x both temporally and spatially, with a maximum lateral force produced at time points 0/10, 1/10 and 2/10, at a position close to 80 % of the

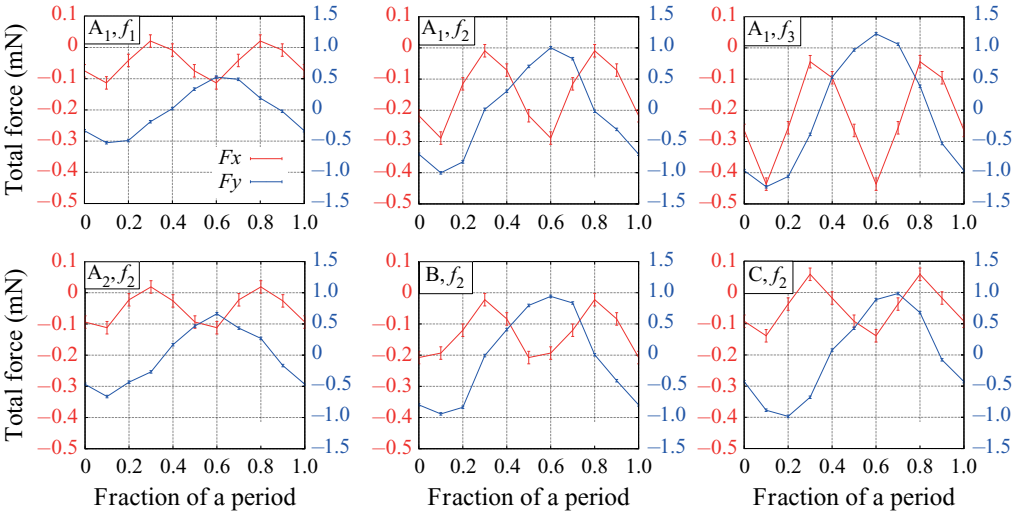

FIGURE 7. Total forces (in mN) acting on the fin, at five time points equidistant over half a period (thrust and lateral forces, in the x and y directions respectively).

fin length. The time points which are typically not associated with thrust production (3/10 and 4/10) correspond to lower lateral forces. The bilobed geometry (shape C) presents a more complex spatio-temporal distribution of F_y, where the force peak alternates between two locations during the half period: at 50 % of the fin length for time points 1/10 and 3/10, and 80 % for time points 2/10 and 4/10. The lowest levels of wasted energy due to lateral forces are found for the long fin at low frequency (shape A_1 at f_1), followed by the shorter fin (shape A_2). The time evolution of the total lateral force is shown in blue in figure 7. The left and right strokes produce mirroring force profiles due to the motion symmetry.

As a measure of propulsive energy, we use η, the ratio between the energy employed to produce thrust and the sum of that energy with the energy employed to produce lateral forces (2.8). Figure 8 allows us to compare the efficiency thus defined for all foils with their respective flapping rates, as a function of St_r and St. David *et al.* (2017) have raised the question of whether or not the Strouhal number calculated from the tip excursion amplitude is a good metric for the width of a vortex wake. They showed that for highly flexible foils, the width of the wake is overestimated by the large tip excursion, and that a rigid projection of the pitching peduncle approximates better the vortices spacing. Interestingly, the fact that flexible fins have larger tip excursion amplitudes than their rigid counterparts is not verified in all our experiments. It is true for geometries A_1 and A_2, but not for shapes B and C, where the amplitude is smaller than the rigid projection. Therefore, in some cases, the flexibility of a fin tends to decrease its excursion amplitude and its Strouhal number.

The most efficient shape is the wider foil (B), followed by the long narrow shape (A_1), which is equally efficient at frequencies f_2 and f_3 but drops in efficiency at lower frequency (f_1). The shorter fins are the less efficient ones, with the lowest value of η found for the short fin with a bilobed edge (C). This is consistent with the fact that flexible fins are typically more efficient than their rigid counterparts (Dewey *et al.* 2013). Indeed, shapes A_2 and C, because of their specific geometries, behave almost like rigid panels, as can be inferred from the close to zero phase lag between the peduncle and the tip angles (table 2), and from the visualization of their midlines (figure 4).

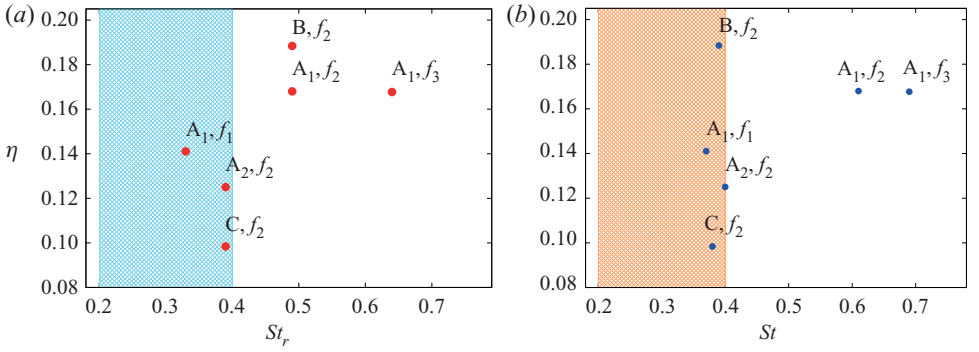

FIGURE 8. Efficiency ratio (as defined by (2.8)), as a function of the rigid Strouhal number St_r, calculated based on the rigid projection of the peduncle (*a*) and the flexible Strouhal number St, calculated based on the tip excursion amplitude of the flexible foils (*b*).

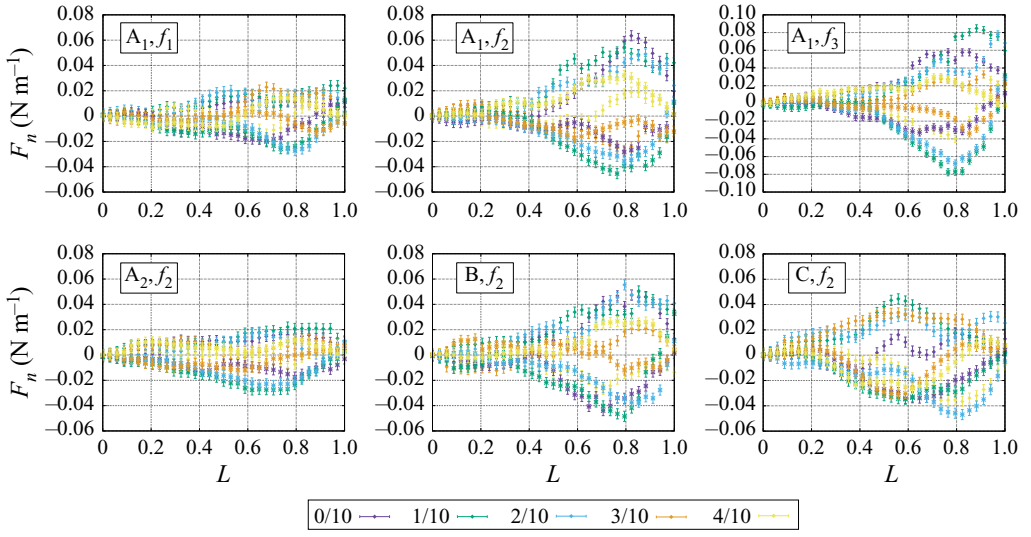

FIGURE 9. Normal force per unit length (in N m^{-1}), acting on both sides of the fin (left side: diamonds, right side: stars) at five time points equidistant over half a period.

In figure 8, the dashed regions denote the range of Strouhal numbers typically associated with efficient thrust production. Interestingly, the classification based on the definition of η shows that shape A$_1$ at frequencies f_2 and f_3 is more efficient than shapes A$_2$ and C, even though their Strouhal numbers lie outside of the usual window of efficiency [0.2,0.4]. In all cases, the efficiency ratio η remains below 0.2, indicating that less than 20 % of the input power is used for propelling the system in the upstream direction, which is not particularly efficient.

The normal force distributions (per unit length) on both sides the hydrofoils are illustrated in figure 9. A low flapping rate (shape A$_1$ at f_1) or a shorter fin length (shape A$_2$) results in lower normal forces across both surfaces, peaking close to 70 % of the total fin length. At intermediate or higher flapping rate (shape A$_1$ at f_2 or f_3), when the fin is wider (shape B), or when the edge is bilobed (shape C), the normal forces increase and the maximum magnitude is shifted close to 80 % of the fin. Moreover, the asymmetry between

the left and right sides of the hydrofoils becomes more important. The magnitudes are asymmetric, and in the most extreme cases, the normal force has the same sign on both fin sides (see for example time points 3/10 and 4/10 for shape A_1 at f_2). These asymmetries translate into larger internal tension within the material. If the sum of the forces on both sides is positive, the material inside the fin is subjected to an outward stretching as it experiences a net force in the direction of the outward normal. Contrarily, if the sum on both sides is negative, the resultant force points towards the inside of the fin, which is then subjected to a net compression. A perfectly symmetric force distribution on both sides (sum equal to zero) would indicate that one side is pulled while the other is pushed with the exact same magnitude, therefore, the hydrodynamic stress would result in the acceleration of the foil, with no internal stress caused by the net external contact forces. To evaluate the spatial distribution of internal tension across the hydrofoils, the normal stress is averaged over a full cycle of flapping, with its sign. The results are presented as colour maps in figure 10. Negative values denote an excess of compression over the oscillation cycle, positive values denote stretching. All membranes experience an overall stretching over the tip region. The most extreme occurrence of that effect is found at the tip of shape A_1 at f_3. A high concentration of stretching is also seen for shape A_1 at f_2, localized in the very centre of the tip, and for shape B, where the concentration zone is shifted to the corners. Additionally, there is a compression zone located distally to the centre of the foils, between approximately 50 % and 75 % of the total length. This is seen in all cases except for shape A_1 at f_2, where the internal compression is relaxed in the centre of the fin. Furthermore, the normal stress distributions are averaged over a period, in absolute values, revealing which portions of the fin are most prominently involved in the production of hydrodynamic forces. These spatial distributions are presented in figure 11, with stress curves covering the dorso-ventral axes of the fin and taken at different locations across its length (25 %, 50 %, 75 % and 100 %). The maximum values are always found at ∼75 % of the foil length. The variations across the surface are marked mostly in the case of the long and narrow geometry (shape A_1), where the curves at $0.25L$, $0.5L$, $0.75L$ and L become more and more separated as the flapping frequency increases. It is noteworthy that a special stress pattern emerges for shape A_1 at f_2, where the curve at $0.75L$ adopts a bilobed signature, not observed for f_1 nor f_3. The excess of normal stress on the tip corners of shape B is also visible in the corresponding graph (stress curve at L). Finally, all fin geometries and flapping rates result in lower levels of hydrodynamic forces generated at the lateral edges (dorsal and ventral) of the hydrofoils.

3.3. *Vorticity fields and wake structures*

The vorticity field ($\boldsymbol{\omega} = \boldsymbol{\nabla} \times \boldsymbol{u}$) is very informative about characteristic flow structures, revealing relations between wake topology, surface distributions of fluid forces and propulsive efficiency. To allow for comparison with previous work, we present the distributions of ω_z, the z component of the vorticity, in 2-D planes intersecting the fins at mid-span. Instantaneous ω_z maps are shown in figure 12, as the foils are crossing the $y = 0$ axis (corresponding to 2/10 of a period, colour coded in pale blue in figures 4–6 and 9). Period-averaged ω_z maps are shown in figure 13.

During the flapping cycle, the instant when the fins cross the $y = 0$ axis occurs between the points of maximal and minimal thrust production (see figure 7). Figure 12 illustrates that a vortex with a core of negative ω_z (rotating clockwise) forms at the tip of each fin. For shape A_1 at frequency f_1, the vortex is almost detached at this point, whereas at f_2, it is fully detached, with a second smaller vortex forming at the tip. The size and strength of these clockwise vortices correlate with propulsive efficiency: the largest vortices, with

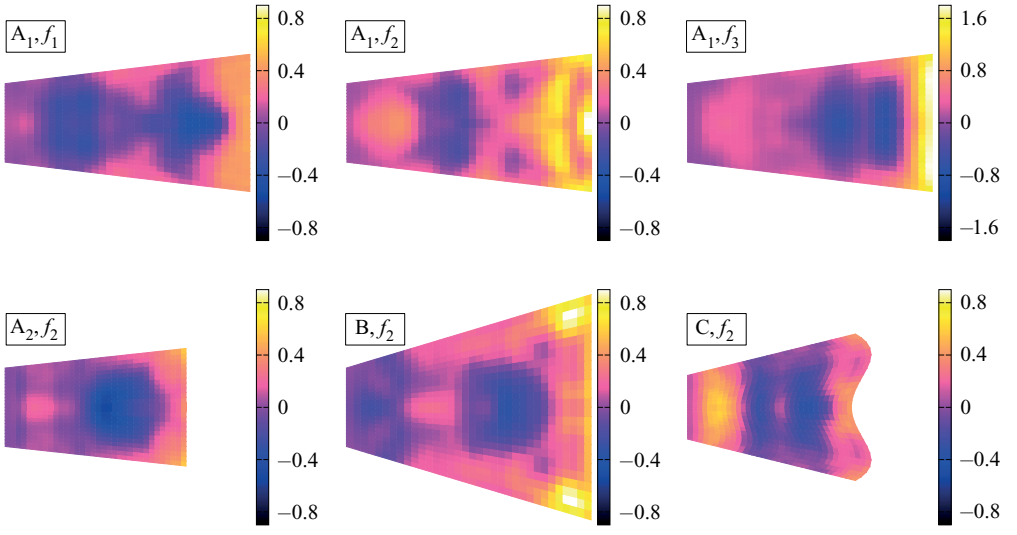

FIGURE 10. Period-averaged signed value of the normal stress acting on the sides of the fin (in Pa).

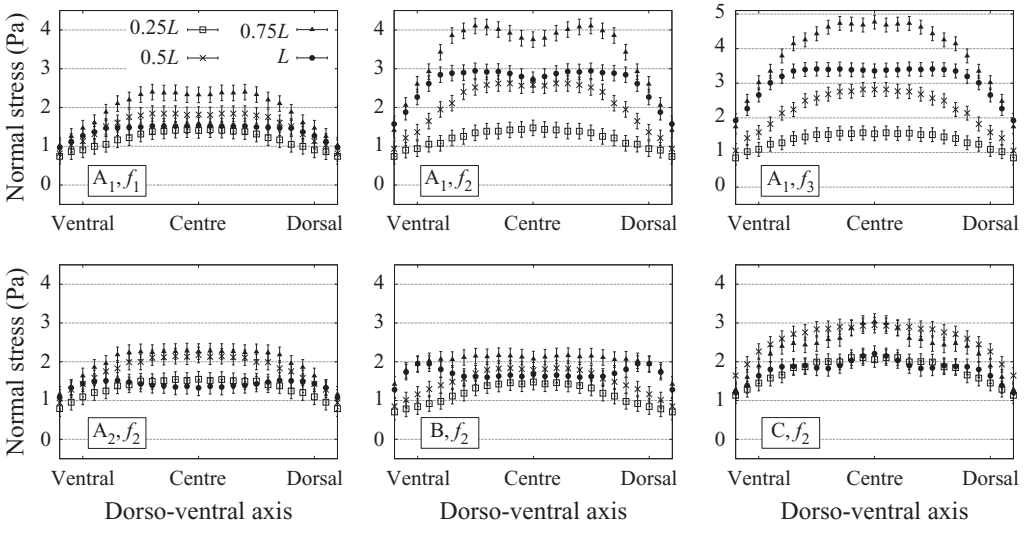

FIGURE 11. Period-averaged absolute value of the normal stress acting on the sides of the fin (in Pa, $\sigma_p = 0.2$ Pa).

maximal $|\omega_z|$ of the order of 50 s^{-1}, are found for shape A_1 at f_2, shape A_1 at f_3 and shape B at f_2, the three cases with maximal η coefficients. Counterclockwise vortices are also present in the snapshot vorticity fields for shapes A_1 (at f_3), A_2, B and C. They are located more downstream as they have been shed during the precedent half-cycle of motion. In the lower frequency cases for shape A_1 (f_1 and f_2), they are not discernible in the field of view, most likely because they have been shed downstream past $x = 35$ mm by that time. The persistence in the close downstream wake of these positive ω_z vortices do not appear to be correlated with propulsive efficiency, nor their magnitude or orientation. Rather, it

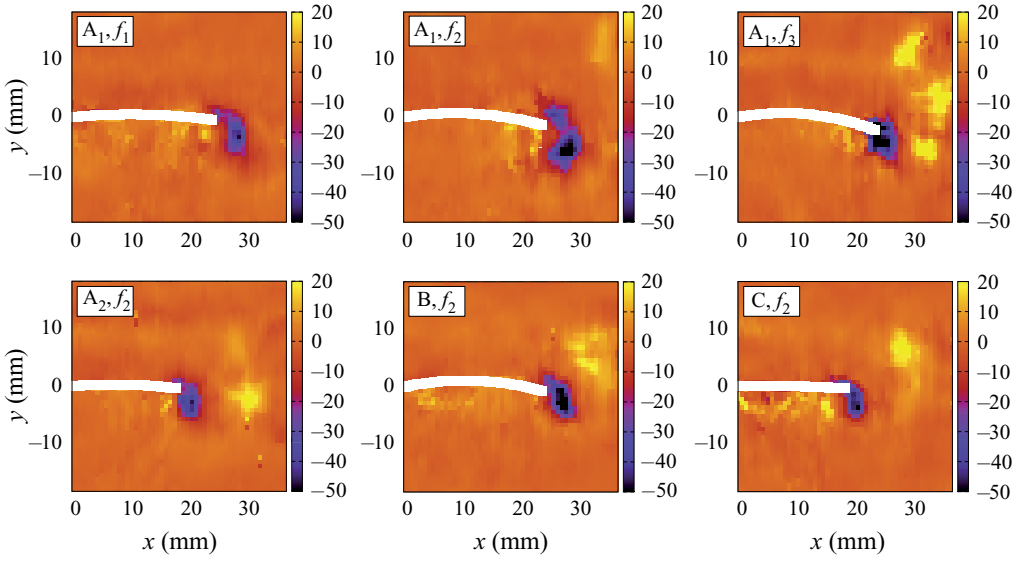

FIGURE 12. Snapshots of ω_z, the z-component of the vorticity field (in s^{-1}) in the plane intersecting the fins half-way through their span, as they are crossing the $y = 0$ axis, travelling towards positive y.

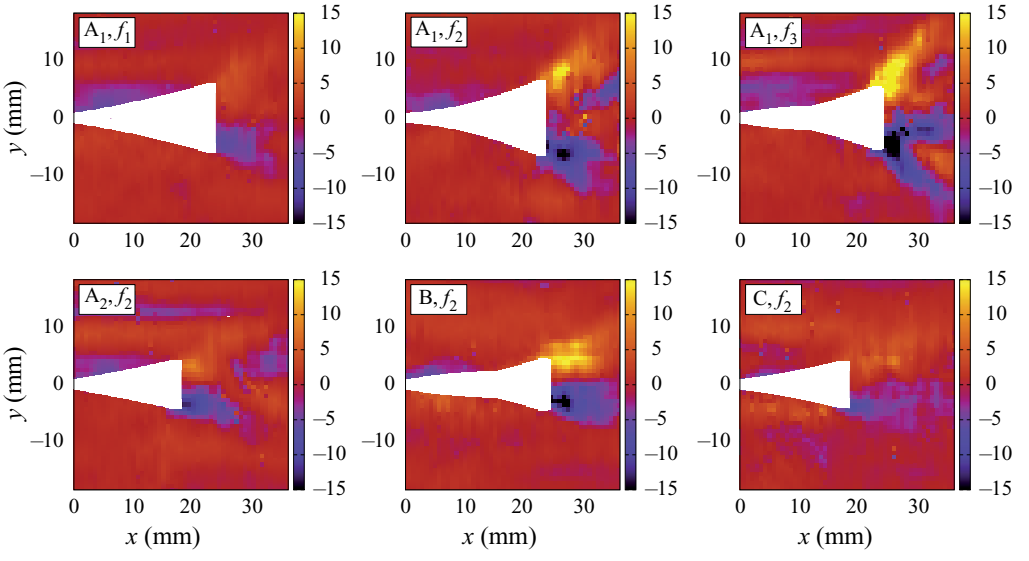

FIGURE 13. Period average of ω_z, the z-component of the vorticity field (in s^{-1}) in the plane intersecting the fins half-way through their span, with the cycle of motion envelopes indicated by white areas.

is the flow structures directly adjacent to the tip which embody the capacity of a fin to generate efficient thrust. It is interesting to observe that the curvature of the trailing edge has an impact on the position at which the vortices are being shed. Indeed, counter-rotating vortices are added to the wake along the $y = 0$ axis for a straight edge geometry (shape A_2), whereas they are detaching at higher y positions for a bilobed trailing edge (shape C).

The period-averaged z-vorticity also presents a correlation with propulsive efficiency: the three hydrofoils with highest η coefficients (shape A_1 at f_2 and f_3 and shape B at f_2) display the highest means, approximately 15 s^{-1} (figure 13). For all shapes and frequencies, the period-averaged ω_z indicates that a surplus of clockwise vorticity is induced at the tip when the fin travels in the $y < 0$ region, and *vice versa*. In other words, the fluid tends to rotate more towards the exterior of the motion envelope close to the tip. In the wake surrounding more proximal portions of the foils, the opposite effect is observed: the period-averaged z-vorticity is slightly positive in the $y < 0$ region, and *vice versa*. This phenomenon is linked to the period-averaged surface maps of normal stress (figure 10), denoting an excess of stretching close to the tip, and a surplus of compression towards the centre and more proximal surface regions. Moreover, a stronger stretching force at the tip appears to be related to higher mean vorticity close to the trailing edge, as seen for shape A_1 at f_2 and f_3 and shape B at f_2. From figure 13, an estimation of the vortex shedding angle can be drawn, corresponding to the opening angle of the maximal $|\omega_z|$ zone. This angle is wider in the cases of shape A_1 at f_2 and f_3, roughly following the tip curvature of the motion envelopes. The most efficient fin (shape B) presents a less pronounced shedding angle, which remains aligned with the motion envelope outline. The shedding angle seems particularly constrained for the two shorter fins behaving more like rigid panels (shapes A_2 and C), which are also the least thrust-efficient hydrofoils. In those cases, the high vorticity areas are almost aligned with the $y = 0$ axis. When comparing the period-averaged wake signatures of shape A_1 at f_1, f_2 and f_3, we observe that increasing the flapping frequency results in the appearance of a reversed circulation area in the downstream wake, close to $x = 33$ mm, where ω_z changes its sign. This mean vorticity reversal does not seem related to propulsive efficiency, since it is also slightly visible in the case of shape A_2 at f_2, one of the least efficient foils in terms of thrust production.

4. Discussion and outlook

We have established a systematic experimental approach to compare the hydrodynamic stress maps on different fin shapes with varying flapping frequency, allowing us to identify the effects of each parameter on the spatio-temporal distributions of fluid forces, and link them to the direct wake topology. In our analysis, we payed special attention to the ability of each hydrofoil to generate thrust (force propelling the system upstream), lateral forces (not contributing to propulsion) and the resulting propulsion efficiency. We also investigated the spatial distributions of external contact forces normal to the fins surfaces and the corresponding internal tension accumulating within the material. We have found that the long narrow geometry generates the most thrust (at equal frequency), and that increasing the flapping frequency increases thrust. Between both short geometries, the bilobed trailing edge allows us to produce slightly more thrust than the straight edge, but only temporarily during the period. At a certain point during the flapping cycle, it is also pushed downstream by the fluid (the opposite of propulsive thrust). It is typically the distal region of the fins which participates more in thrust generation, except for the short bilobed geometry whose central portion is the one most involved. As for the lateral forces, detrimental to propulsive efficiency, the short straight geometry (at equal frequency) reaches the lowest levels. For the long geometry, reducing the flapping frequency also reduces the lateral force magnitude throughout the cycle.

The examination of instantaneous and period-averaged vorticity fields yielded the conclusion that the formation of larger and stronger vortices directly at the tip as well as the accumulation of excess vorticity close to the trailing edge over a full period are related to better propulsive efficiency. Among all cases tested, the most efficient geometry was

found to be the long wide fin, followed by the long narrow one, whose efficiency remained similar at higher frequency but dropped significantly at the lowest one. The least efficient fin morphology is the short fin with bilobed trailing edge. This type of tip curvature is ubiquitous in nature. It is interesting, both for the study of biological swimmers and for the design of artificial fins, to discover that the naturally widespread bilobed shape does not improve efficiency nor does it grant more thrust producing capabilities to a simple fin model at Reynolds numbers which are on the low side of the inertial regime. It is more likely that an authentic fish fin with a bilobed trailing edge is coupled with specific elasticity profiles and complex controlled motion programs, in order to achieve its functional role. It could also be that the advantages of this tip curvature appear only for a specific combination of parameters such as length and flapping frequency. Besides, we have observed that the bilobed geometry results in a dynamical shift of fluid force peaks along the fin length during the stroke cycle. This more complex dynamics of force distributions could be used actively by an appendage to achieve fine manoeuvres. The external contact forces from the fluid acting normally on both foils surfaces result in an accumulation of internal tension throughout the flapping cycle. The fin tip is subjected to an excess of tissue stretching, an effect which becomes more important as the foil becomes longer, or as it flaps faster. The stretching tension concentrates towards the tip corners for a wider geometry. Moreover, the foil membranes experience an overall compression zone at approximately two thirds of their total length. Interestingly, in the case of the long narrow geometry, flapping at frequency f_2, this compression region partly disappears. In that specific case, a particular stress pattern emerges from 75 % of the total length up to the tip, where the normal stress (averaged in absolute value over a period) presents a double peak signature. For all fin geometries, the period-averaged absolute value of the normal stress reaches its maximum at approximately 75 % of the total length. These stress maps are very indicative of how the fin architecture must be conceived in order to withstand specific concentrations of mechanical loads and internal tension throughout its oscillation cycle.

The flexible tails of rayed-fin fishes display an impressively wide range of morphological traits and provide a great model system to study the relation between fin geometry and propulsive efficiency (Affleck 1950; McNeill 1974; Lauder 1989; Weihs 1989; Lauder 2000; Lauder & Madden 2007; Blake, Li & Chan 2009; Flammang *et al.* 2011*b*). Complex combinations of environmental constraints participate in the selective evolution of fish fins, and the resulting elastic properties, geometry and kinematics of each specie constitute an elegant compromise between competing survival demands such as the necessity to achieve fine control of the fin surface for delicate manoeuvring, to generate quick acceleration bursts or to maintain long distance efficiency (Webb 1975; Lauder & Liem 1983; Lauder 1989, 2006, 2015). It is tempting to assume that evolution has optimized the geometric and kinematic parameters of fins to meet with the functional demands of distinct habitats. However, drawing a parallel between form and function requires taking into account the evolutionary history of fins morphologies, and considering not only the external shape, but also internal structures, in order to avoid mistaking correlations between morphology, habitat and function for causal relationships (Lauder & Liem 1983; Lauder 1989). Previous investigations on the interplay between shape and stiffness of fin models and their capacity to generate thrust efficiently have already demonstrated that efficiency varies in a complex manner as a function of the different fin attributes, and that it is not a simple matter to identify an optimal shape (Feilich & Lauder 2015). Rather, efficiency can be maximized by several combinations of parameters, depending on the flow conditions, and it remains a great challenge to draw general conclusions about the functional advantages of geometrical and kinematic

aspects. The present work illustrates how the investigation of hydrodynamic stresses based on three-dimensional PTV experiments can provide precious information about the mechanical interplay between a fin-like structure and the surrounding fluid. It paves the way for future experimental studies using direct evaluation of fluid forces on the surface of submerged flexible appendages, allowing us to tackle directly the fundamental problem of form and function in the context of propulsion through a fluid medium. To conclude, the possibility of resolving the 3-D instantaneous hydrodynamic stress fields on small-scale models of deformable structures opens the door to many applications in the engineering design of aeronautic and aquatic vehicles or the field of biophysics concerned with animal locomotion.

Acknowledgements

This work was funded by the Swiss National Science Foundation (SNF) via a Sinergia research grant as well as a UZH Forschungskredit Candoc grant. We are grateful for interdisciplinary discussions with T. Aegerter, A. Jaźwińska, I. Kicic, S. Puri and S. Verma. We are very thankful to J. O. Dabiri *et al.* for making the queen2 pressure algorithm available (Dabiri *et al.* 2014).

Declaration of interests

The authors report no conflict of interest.

REFERENCES

Affleck, R. J. 1950 Some points in the function, development and evolution of the tail in fishes. *Proc. Zool. Soc. Lond.* **120** (2), 349–368.

Aris, R. 1990 *Vectors, Tensors and the Basic Equations of Fluid Mechanics*. Dover.

Arnal, D. 1984 Description and prediction of transition in two-dimensional, incompressible flow. In *Special Course on Stability and Transition of Laminar Flow* (ed. AGARD-R-709). Defense Technical Information Center.

Bainbridge, R. 1960 Speed and stamina in three fish. *J. Expl Biol.* **37** (1), 129–153.

Baur, T. & Köngeter, J. 1999 PIV with high temporal resolution for the determination of local pressure reductions from coherent turbulence phenomena. In *3rd International Workshop on PIV, Santa Barbara, USA*, pp. 101–106.

Blake, R. W., Li, J. & Chan, K. H. S. 2009 Swimming in four goldfish Carassius auratus morphotypes: understanding functional design and performance employing artificially selected forms. *J. Fish Biol.* **75** (3), 591–617.

Blickhan, R., Krick, C., Zehren, D., Nachtigall, W. & Breithaupt, T. 1992 Generation of a vortex chain in the wake of a suhundulatory swimmer. *Naturwissenschaften* **79**, 220–221.

Bohl, D. G. & Koochesfahani, M. M. 2009 MTV measurements of the vortical field in the wake of an airfoil oscillating at high reduced frequency. *J. Fluid Mech.* **620**, 63–88.

Bohlen, J., Petrtyl, M., Petra, C. & Chhouk, B. 2016 Schistura kampucheensis, a new species of loach from Cambodia (Teleostei: Nemacheilidae). *Ichthyol. Expl Freshwat.* **26**, 353–362.

Bozkurttas, M., Dong, H., Mittal, R., Madden, P. & Lauder, G. V. 2006 Hydrodynamic performance of deformable fish fins and flapping foils. In *44th AIAA Aerospace Sciences Meeting and Exhibit*. Available at: https://arc.aiaa.org/doi/pdf/10.2514/6.2006-1392.

Bozkurttas, M., Mittal, R., Dong, H., Lauder, G. V. & Madden, P. 2009 Low-dimensional models and performance scaling of a highly deformable fish pectoral fin. *J. Fluid Mech.* **631**, 311–342.

Buchholz, J. & Smits, A. 2006 On the evolution of the wake structure produced by a low-aspect-ratio pitching panel. *J. Fluid Mech.* **564**, 433–443.

DABIRI, J. O., BOSE, S., GEMMELL, B., COLIN, S. & COSTELLO, J. 2014 An algorithm to estimate unsteady and quasi-steady pressure fields from velocity field measurements. *J. Expl Biol.* **217**, 331–336.

DAGENAIS, P. & AEGERTER, C. M. 2019 Hydrodynamic stress maps on the surface of a flexible fin-like foil. arXiv:1910.09887.

DAI, H., LUO, H., FERREIRA DE SOUSA, P. & DOYLE, J. 2012 Thrust performance of a flexible low-aspect-ratio pitching plate. *Phys. Fluids* **24**, 101903.

DAVID, L., JARDIN, T., BRAUD, P. & FARCY, A. 2012 Time-resolved scanning tomography PIV measurements around a flapping wing. *Exp. Fluids* **52** (4), 857–864.

DAVID, M. J., GOVARDHAN, R. N. & ARAKERI, J. H. 2017 Thrust generation from pitching foils with flexible trailing edge flaps. *J. Fluid Mech.* **828**, 70–103.

DEWEY, P., BOSCHITSCH, B., MOORED, K., STONE, H. & SMITS, A. 2013 Scaling laws for the thrust production of flexible pitching panels. *J. Fluid Mech.* **732**, 29–46.

DEWEY, P. A., CARRIOU, A. & SMITS, A. J. 2012 On the relationship between efficiency and wake structure of a batoid-inspired oscillating fin. *J. Fluid Mech.* **691**, 245–266.

DRACOS, TH. 1996 *Particle Tracking Velocimetry (PTV)*, pp. 155–160. Springer Netherlands.

DRUCKER, E. G. & LAUDER, G. V. 1999 Locomotor forces on a swimming fish: three-dimensional vortex wake dynamics quantified using digital particle image velocimetry. *J. Expl Biol.* **202** (18), 2393–2412.

DRUCKER, E. G. & LAUDER, G. V. 2001 Locomotor function of the dorsal fin in teleost fishes: experimental analysis of wake forces in sunfish. *J. Expl Biol.* **204** (17), 2943–2958.

DRUCKER, E. G. & LAUDER, G. V. 2005 Locomotor function of the dorsal fin in rainbow trout: kinematic patterns and hydrodynamic forces. *J. Expl Biol.* **208** (23), 4479–4494.

EGAN, B., BROWNELL, C. & MURRAY, M. 2016 Experimental assessment of performance characteristics for pitching flexible propulsors. *J. Fluids Struct.* **67**, 22–33.

ELOY, C. 2012 Optimal Strouhal number for swimming animals. *J. Fluids Struct.* **30**, 205–218.

ELOY, C. 2013 On the best design for undulatory swimming. *J. Fluid Mech.* **717**, 48–89.

ESPOSITO, C. J., TANGORRA, J. L., FLAMMANG, B. E. & LAUDER, G. V. 2012 A robotic fish caudal fin: effects of stiffness and motor program on locomotor performance. *J. Expl Biol.* **215** (1), 56–67.

FEILICH, K. L. & LAUDER, G. V. 2015 Passive mechanical models of fish caudal fins: effects of shape and stiffness on self-propulsion. *Bioinspir. Biomim.* **10**, 036002.

FLAMMANG, B. E., LAUDER, G. V., TROOLIN, D. & STRAND, T. E. 2011*a* Volumetric imaging of fish locomotion. *Biol. Lett.* **7**, 695–8.

FLAMMANG, B. E., LAUDER, G. V., TROOLIN, D. & STRAND, T. E. 2011*b* Volumetric imaging of shark tail hydrodynamics reveals a three-dimensional dual-ring vortex wake structure. *Proc. R. Soc.* B*/Biol. Sci.* **278**, 3670–3678.

FLORYAN, D., VAN BUREN, T., ROWLEY, C. & SMITS, A. 2017 Scaling the propulsive performance of heaving and pitching foils. *J. Fluid Mech.* **822**, 386–397.

FUJISAWA, N., NAKAMURA, Y., MATSUURA, F. & SATO, Y. 2006 Pressure field evaluation in microchannel junction flows through μPIV measurement. *Microfluid Nanofluid* **2** (5), 447–453.

GEERLINK, P. J. & VIDELER, J. 1986 The relation between structure and bending properties of teleost fin rays. *Neth. J. Zool.* **37**, 59–80.

GODOY-DIANA, R., AIDER, J. L. & WESFREID, J. 2008 Transitions in the wake of a flapping foil. *Phys. Rev.* E*: Stat. Nonlinear Soft Matter Phys.* **77**, 016308.

GREEN, M. A., ROWLEY, C. W., SMITS, A. J. 2011 The unsteady three-dimensional wake produced by a trapezoidal pitching panel. *J. Fluid Mech.* **685**, 117–145.

GRESHO, P. M. & SANI, R. L. 1987 On pressure boundary conditions for the incompressible Navier–Stokes equations. *Intl J. Numer. Meth. Fluids* **7** (10), 1111–1145.

GURKA, R., LIBERZON, A., HEFETZ, D., RUBINSTEIN, D. & SHAVIT, U. 1999 Computation of pressure distribution using PIV velocity data. In *Third International Workshop on PIV, Santa Barbara, CA*, pp. 671–676..

INCROPERA, F. P., DEWITT, D. P., BERGMAN, T. L. & LAVINE, A. S. 2007 *Fundamentals of Heat and Mass Transfer*, 6th edn. Wiley.

JAKOBSEN, M., DEWHIRST, T. & GREATED, C. 1999 Particle image velocimetry for predictions of acceleration fields and force within fluid flows. *Meas. Sci. Technol.* **8**, 1502.

JARDIN, T., DAVID, L. & FARCY, A. 2009 Characterization of vortical structures and loads based on time-resolved PIV for asymmetric hovering flapping flight. *Exp. Fluids* **46**, 847–857.

JOSHI, P., LIU, X. & KATZ, J. 2014 Effects of fluctuating pressure gradients on boundary layer turbulence. *J. Fluid Mech.* **748**, 36.

DE KAT, R. & GANAPATHISUBRAMANI, R. B. 2013 Pressure from particle image velocimetry for convective flows: a Taylor's hypothesis approach. *Meas. Sci. Technol.* **24** (2), 024002.

DE KAT, R. & VAN OUDHEUSDEN, B. W. 2012 Instantaneous planar pressure determination from PIV in turbulent flow. *Exp. Fluids* **52** (5), 1089–1106.

KENNEY, J. F. & KEEPING, E. S. 1962 The median, relation between mean, median and mode, relative merits of mean, median and mode. In *Mathematics of Statistics*, 3rd edn, vol. pt. 1. Van Nostrand.

KERN, S. & KOUMOUTSAKOS, P. 2006 Simulations of optimized anguilliform swimming. *J. Expl Biol.* **209** (24), 4841–4857.

KHODARAHMI, I., SHAKERI, M., SHARP, M. & AMINI, A. 2010 Using PIV to determine relative pressures in a stenotic phantom under steady flow based on the pressure-poisson equation. In *Conference proceedings: . . . Annual International Conference of the IEEE Engineering in Medicine and Biology Society*, pp. 2594–2597.

KIM, D. & GHARIB, M. 2010 Experimental study of three-dimensional vortex structures in translating and rotating plates. *Exp. Fluids* **49**, 329–3390.

KOBASHI, Y. & HAYAKAWA, M. 1980 The transition mechanism of an oscillating boundary layer. In *Laminar-Turbulent Transition* (ed. R. Eppler & H. Fasel), pp. 102–109. Springer.

KOTTELAT, M. 2017 Three new species of loaches of the genus *Schistura* from the Nam Ngiep drainage, central Laos (Teleostei: Nemacheilidae). *Raffles Bull. Zool.* **65**, 691–706.

KUNZE, S. & BRÜCKER, C. 2011 Flow control over an undulating membrane. *Exp. Fluids* **50** (3), 747–759.

LAI, W., PAN, G., MENON, R., TROOLIN, D., CASTAÑO-GRAFF, E., GHARIB, M. & PEREIRA, F. J. A. 2008 Volumetric three-component velocimetry: a new tool for 3D flow measurement. In *14th International Symposium on Applications of Laser Techniques to Fluid Mechanics*.

LAUDER, G. V. 1989 Caudal fin locomotion in ray-finned fishes: historical and functional analyses. *Integr. Compar. Biol.* **29** (1), 85–102.

LAUDER, G. V. 2000 Function of the caudal fin during locomotion in fishes: kinematics, flow visualization, and evolutionary patterns. *Am. Zool.* **40** (1), 101–122.

LAUDER, G. V. 2006 Locomotion. In *The Physiology of Fishes* (ed. D. H. Evans & J. B. Claiborne), pp. 3–46. CRC.

LAUDER, G. V. 2015 Flexible fins and fin rays as key transformations in ray-finned fishes. In *Great Transformations in Vertebrate Evolution*, chap. 2. University of Chicago Press.

LAUDER, G. V., ANDERSON, E., TANGORRA, J. & MADDEN, P. 2007 Fish biorobotics: kinematics and hydrodynamics of self-propulsion. *J. Expl Biol.* **210**, 2767–2780.

LAUDER, G. V. & LIEM, K. F. 1983 *The evolution and Interrelationships of the Actinopterygian Fishes*. Bulletin of the Museum of Comparative Zoology at Harvard College.

LAUDER, G. V., MADDEN, P., HUNTER, I., TANGORRA, J., DAVIDSON, N., PROCTOR, L., MITTAL, R., DONG, H. & BOZKURTTAS, M. 2005 Design and performance of a fish fin-like propulsor for AUVs. In *14th International Symposium on Unmanned Untethered Submersible Technology, Durham, NH*.

LAUDER, G. V. & MADDEN, P. G. A. 2007 Fish locomotion: kinematics and hydrodynamics of flexible foil-like fins. *Exp. Fluids* **43**, 641–653.

LENTINK, D. 2008 Exploring the biofluiddynamics of swimming and flight. PhD thesis, Wageningen University.

LINK, O., SANHUEZA, C., ARRIAGADA, P., BREVIS, W., LABORDE, A., GONZÁLEZ, A., WILKES, M. & HABIT, E. 2017 The fish Strouhal number as a criterion for hydraulic fishway design. *Ecol. Engng* **103**, 118–126.

LIU, G., REN, Y., DONG, H., AKANYETI, O., LIAO, J. & LAUDER, G. V. 2017 Computational analysis of vortex dynamics and performance enhancement due to body–fin and fin–fin interactions in fish-like locomotion. *J. Fluid Mech.* **829**, 65–88.

LIU, X. & KATZ, J. 2006 Instantaneous pressure and material acceleration measurements using a four-exposure PIV system. *Exp. Fluids* **41**, 227–240.

LORENZONI, V., TUINSTRA, M., MOORE, P. & SCARANO, F. 2009 *Aeroacoustic Analysis of a Rod-Airfoil Flow by Means of Time-Resolved PIV*. American Institute of Aeronautics and Astronautics.

LOW, K. 2007 Design, development and locomotion control of bio-fish robot with undulating anal fins. *Intl J. Robot. Autom.* **22**, 88–99.

LOW, K. H. & WILLY, A. 2006 Biomimetic motion planning of an undulating robotic fish fin. *J. Vib. Control* **12**, 1337–1359.

LUCAS, K. N., DABIRI, J. O. & LAUDER, G. V. 2017 A pressure-based force and torque prediction technique for the study of fish-like swimming. *PLoS ONE* **12**, e0189225.

LUCAS, K., THORNYCROFT, P., GEMMELL, B., COLIN, S., COSTELLO, J. & LAUDER, G. 2015 Effects of non-uniform stiffness on the swimming performance of a passively-flexing, fish-like foil model. *Bioinspir. Biomim.* **10**, doi:10.1088/1748-3190/10/5/056019.

MAAS, H. G., GRUEN, A. & PAPANTONIOU, D. 1993 Particle tracking velocimetry in three-dimensional flows. *Exp. Fluids* **15** (2), 133–146.

MARAIS, C., THIRIA, B., WESFREID, J. & GODOY-DIANA, R. 2012 Stabilizing effect of flexibility in the wake of a flapping foil. *J. Fluid Mech.* **710**, 659–669.

MCCLURE, J. & YARUSEVYCH, S. 2017 Optimization of planar PIV-based pressure estimates in laminar and turbulent wakes. *Exp. Fluids* **58**, 62.

MCHENRY, M. J. & LAUDER, G. V. 2005 The mechanical scaling of coasting in zebrafish (Danio rerio). *J. Expl Biol.* **208** (12), 2289–2301.

MCNEILL, A. R. 1974 *Functional Design in Fishes*. Hutchinson.

MITTAL, R., DONG, H., BOZKURTTAS, M., LAUDER, G. V. & MADDEN, P. 2006 Locomotion with flexible propulsors: II. Computational modeling of pectoral fin swimming in sunfish. *Bioinspir. Biomim.* **1** (4), S35–S41.

MUIR, R. E., ARREDONDO-GALEANA, A. & VIOLA, I. M. 2017 The leading-edge vortex of swift wing-shaped delta wings. *R. Soc. Open Sci.* **4**, 170077.

MÜLLER, U. K., VAN DEN BOOGAART, J. G. M. & VAN LEEUWEN, J. L. 2008 Flow patterns of larval fish: undulatory swimming in the intermediate flow regime. *J. Expl Biol.* **211** (2), 196–205.

MÜLLER, U. K., SMIT, J., STAMHUIS, E. J., VIDELER, J. J. 2001 How the body contributes to the wake in undulatory fish swimming: flow fields of a swimming eel (Anguilla anguilla). *J. Expl Biol.* **204**, 2751–62.

MÜLLER, U. K., STAMHUIS, E. J. & VIDELER, J. J. 2000 Hydrodynamics of unsteady fish swimming and the effects of body size: comparing the flow fields of fish larvae and adults. *J. Expl Biol.* **203**, 193–206.

MÜLLER, U. K., VAN DEN HEUVEL, B., STAMHUIS, E. J. & VIDELER, J. J. 1997 Fish foot prints: morphology and energetics of the wake behind a continuously swimming mullet (Chelon labrosus Risso). *J. Expl Biol.* **200**, 2893–906.

MÜLLER, U. K. & VAN LEEUWEN, J. L. 2006 Undulatory fish swimming: from muscles to flow. *Fish Fish.* **7**, 84–103.

MURAI, Y., NAKADA, T., SUZUKI, T. & YAMAMOTO, F. 2007 Particle tracking velocimetry applied to estimate the pressure field around a Savonius turbine. *Meas. Sci. Technol.* **18**, 2491.

MWAFFO, V., ZHANG, P., ROMERO CRUZ, S. & PORFIRI, M. 2017 Zebrafish swimming in the flow: a particle image velocimetry study. *PeerJ* **5**, e4041.

NARUSE, K., TANAKA, M. & TAKEDA, H. 2011 *Medaka: A Model for Organogenesis, Human Disease, and Evolution*. Springer.

NAUEN, J. C. & LAUDER, G. V. 2002*a* Hydrodynamics of caudal fin locomotion by chub mackerel, *Scomber Japonicus* (Scombridae). *J. Expl Biol.* **205** (12), 1709–1724.

NAUEN, J. C. & LAUDER, G. V. 2002*b* Quantification of the wake of rainbow trout (*Oncorhynchus mykiss*) using three-dimensional stereoscopic digital particle image velocimetry. *J. Expl Biol.* **205** (21), 3271–3279.

OBREMSKI, H. J. & FEJER, A. A. 1967 Transition in oscillating boundary layer flows. *J. Fluid Mech.* **29** (1), 93–111.

OFFEN, N., BLUM, N., MEYER, A. & BEGEMANN, G. 2008 Fgfr1 signalling in the development of a sexually selected trait in vertebrates, the sword of swordtail fish. *BMC Develop. Biol.* **8**, 98.

VAN OUDHEUSDEN, B. W. 2008 Principles and application of velocimetry-based planar pressure imaging in compressible flows with shocks. *Exp. Fluids* **45** (4), 657–674.

VAN OUDHEUSDEN, B. W. 2013 PIV-based pressure measurement. *Meas. Sci. Technol.* **24** (3), 032001.

VAN OUDHEUSDEN, B. W., SCARANO, F. & CASIMIRI, E. W. F. 2006 Non-intrusive load characterization of an airfoil using PIV. *Exp. Fluids* **40** (6), 988–992.

VAN OUDHEUSDEN, B. W., SCARANO, F., ROOSENBOOM, E. W. M., CASIMIRI, E. W. F. & SOUVEREIN, L. J. 2007 Evaluation of integral forces and pressure fields from planar velocimetry data for incompressible and compressible flows. *Exp. Fluids* **43** (2), 153–162.

PALSTRA, A. P., TUDORACHE, C., ROVIRA, M., BRITTIJN, S. A., BURGERHOUT, E., VAN DEN THILLART, G. E. E. J. M., SPAINK, H. P. & PLANAS, J. V. 2010 Establishing zebrafish as a novel exercise model: swimming economy, swimming-enhanced growth and muscle growth marker gene expression. *PLoS ONE* **5** (12), e14483.

PANCIROLI, R. & PORFIRI, M. 2013 Evaluation of the pressure field on a rigid body entering a quiescent fluid through particle image velocimetry. *Exp. Fluids* **54** (12), 1630.

PARICHY, D. M., ELIZONDO, M. R., MILLS, M., GORDON, T. N. & ENGESZER, R. E. 2009 Normal table of post-embryonic zebrafish development: staging by externally visible anatomy of the living fish. *Develop. Dyn.* **238**, 2975–3015.

PEREIRA, F. J. A., STÜER, H., GRAFF, E. C. & GHARIB, M. 2006 Two-frame 3D particle tracking. *Meas. Sci. Technol.* **17**, 1680–1692.

PLONGSESTHEE, R., BEAMISH, F. & PAGE, L. 2012 Sexual dimorphism in species of *Schistura* (Teleostei: Nemacheilidae) from the Mae Khlong basin and peninsular Thailand. *Zootaxa* **3586**, 353–358.

PRANDTL, L. 1952 *Essentials of Fluid Dynamics: With Applications to Hydraulics Aeronautics, Meteorology, and Other Subjects*. Hafner.

PURI, S. 2018 Approaching zebrafish (Danio rerio) caudal fin regeneration from a biomechanical perspective. PhD thesis, University of Zurich.

PURI, S., AEGERTER-WILMSEN, T., JAŹWIŃSKA, A. & AEGERTER, C. M. 2018 In vivo quantification of mechanical properties of caudal fins in adult zebrafish. *J. Expl Biol.* **221** (4), jeb171777.

QING PING, W., WANG, S., DONG, X., SHANG, L. J. & TAN, M. 2013 Design and kinetic analysis of a biomimetic underwater vehicle with two undulating long-fins. *Acta Automat. Sinica* **39** (8), 1330–1338.

QUINN, D., LAUDER, G. V. & SMITS, A. 2014 Scaling the propulsive performance of heaving flexible panels. *J. Fluid Mech.* **738**, 250–267.

QUINN, D., LAUDER, G. V. & SMITS, A. 2015 Maximizing the efficiency of a flexible propulsor using experimental optimization. *J. Fluid Mech.* **767**, 430–448.

RAFFEL, M., WILLERT, C. E., WERELEY, S. & KOMPENHANS, J. 1998 *Particle Image Velocimetry: A Practical Guide*. Springer.

RAGNI, D., VAN OUDHEUSDEN, B. W. & SCARANO, F. 2012 3D pressure imaging of an aircraft propeller blade-tip flow by phase-locked stereoscopic PIV. *ACM J. Expl Algorithms* **52**, 463–477.

REN, Z., HU, K., WANG, T. & WEN, L. 2016*a* Investigation of fish caudal fin locomotion using a bio-inspired robotic model. *Intl J. Adv. Robot. Syst.* **13** (3), 87.

REN, Z., YANG, X., WANG, T. & WEN, L. 2016*b* Hydrodynamics of a robotic fish tail: effects of the caudal peduncle, fin ray motions and the flow speed. *Bioinspir. Biomim.* **11**, 016008.

ROSIC, M., THORNYCROFT, P., FEILICH, K., LUCAS, K. & LAUDER, G. V. 2017 Performance variation due to stiffness in a tuna-inspired flexible foil model. *Bioinspir. Biomim.* **12**, 016011.

SAMBILAY, V. C. JR. 2005 Interrelationships between swimming speed, caudal fin aspect ratio and body length of fishes. *Fishbyte* **8**, 16–20.

SHELTON, R. M., THORNYCROFT, P. J. M. & LAUDER, G. V. 2014 Undulatory locomotion of flexible foils as biomimetic models for understanding fish propulsion. *J. Expl Biol.* **217** (12), 2110–2120.

SHINDE, S. & ARAKERI, J. H. 2014 Flexibility in flapping foil suppresses meandering of induced jet in absence of free stream. *J. Fluid Mech.* **757**, 231–250.

STAMHUIS, E. & VIDELER, J. 1995 Quantitative flow analysis around aquatic animals using laser sheet particle image velocimetry. *J. Expl Biol.* **198** (2), 283–294.

TANGORRA, J. L., DAVIDSON, S. N., HUNTER, I. W., MADDEN, P. G. A., LAUDER, G. V., DONG, H., BOZKURTTAS, M. & MITTAL, R. 2007 The development of a biologically inspired propulsor for unmanned underwater vehicles. *IEEE J. Ocean. Engng* **32** (3), 533–550.

TANGORRA, J. L., LAUDER, G. V., HUNTER, I. W., MITTAL, R., MADDEN, P. G. A. & BOZKURTTAS, M. 2010 The effect of fin ray flexural rigidity on the propulsive forces generated by a biorobotic fish pectoral fin. *J. Expl Biol.* **213** (23), 4043–4054.

TAYLOR, G. K., NUDDS, R. L. & THOMAS, A. L. R. 2003 Flying and swimming animals cruise at a Strouhal number tuned for high power efficiency. *Nature* **425** (6959), 707–711.

TRIANTAFYLLOU, M., TECHET, A. & HOVER, F. 2004 Review of experimental work in biomimetic foils. *IEEE J. Ocean. Engng* **29**, 585–594.

TRIANTAFYLLOU, M., TRIANTAFYLLOU, G. & YUE, D. K. P. 2000 Hydrodynamics of fishlike swimming. *ARFM* **32**, 33–53.

TRONCHIN, T., DAVID, L. & FARCY, A. 2015 Loads and pressure evaluation of the flow around a flapping wing from instantaneous 3D velocity measurements. *Exp. Fluids* **56** (1), 7.

TYTELL, E. D. 2006 Median fin function in bluegill sunfish lepomis macrochirus: streamwise vortex structure during steady swimming. *J. Expl Biol.* **209** (8), 1516–1534.

TYTELL, E. D., STANDEN, E. M. & LAUDER, G. V. 2008 Escaping flatland: three-dimensional kinematics and hydrodynamics of median fins in fishes. *J. Expl Biol.* **211** (2), 187–195.

VAN LEEUWEN, J. L., VOESENEK, C. & MÜLLER, U. 2015 How body torque and Strouhal number change with swimming speed and developmental stage in larval zebrafish. *J. R. Soc. Interface* **12**, 20150479.

VIDELER, J. 1975 On the interrelationships between morphology and movement in the tail of the cichlid fish *Tilapia nilotica* (L.). *Neth. J. Zool.* **25**, 143–194.

VIOLATO, D., MOORE, P. & SCARANO, F. 2011 Lagrangian and Eulerian pressure field evaluation of rod-airfoil flow from time-resolved tomographic PIV. *Exp. Fluids* **50** (4), 1057–1070.

VOGEL, S. 1994 *Life in Moving Fluids*. Princeton University Press.

WANG, Z., GAO, Q., WEI, R. & WANG, J. 2017 Error propagation in the procedure of pressure reconstruction based on PIV data. *J. Phys.: Conf. Ser.* **822**, 012055.

WARDLE, C. S. 1975 Limit of fish swimming speed. *Nature* **255**, 725–727.

WEBB, P. W. 1975 *Hydrodynamics and Energetics of Fish Propulsion*. Department of the Environment Fisheries and Marine Service.

WEERDEN, J., REID, D. & HEMELRIJK, C. 2013 A meta-analysis of steady undulatory swimming. *Fish Fish.* **15**, 397–409.

WEIHS, D. 1989 Design features and mechanics of axial locomotion in fish. *Am. Zool.* **29** (1), 151–160.

WHITAKER, S. 1968 *Introduction Fluid Mechanics*. Prentice-Hall.

WINDSOR, S. P. 2008 Hydrodynamic imaging by blind Mexican cave fish. PhD thesis, University of Auckland.

XIONG, G. & LAUDER, G. V. 2014 Center of mass motion in swimming fish: effects of speed and locomotor mode during undulatory propulsion. *Zoology* **117** (4), 269–281.

YATES, G. T. 1983 Hydrodynamics of body and caudal fin propulsion. In *Fish Biomechanics*, pp. 177–213. Praeger.

ZHOU, C. & LOW, K. H. 2012 Design and locomotion control of a biomimetic underwater vehicle with fin propulsion. *IEEE-ASME Trans. Mechatron.* **17**, 25–35.

ZHU, R., WANG, J., LEWIS, G., ZHU, J., DONG, H., BART-SMITH, H., WAINWRIGHT, D. & LAUDER, G. V. 2017 Propulsive performance of pitching panels with bio-inspired passive directional flexibility. *AIAA Paper* 2017-3980.